PCCP

Accepted Manuscript

This article can be cited before page numbers have been issued, to do this please use: J. Fowlkes, B. Geier, B. Lewis, P. Rack, M. Stanford, R. Winkler and H. Plank, *Phys. Chem. Chem. Phys.*, 2015, DOI: 10.1039/C5CP01196E.

View Article Online
DOI: 10.1039/C5CP01196E

Journal Name

RSCPublishing

ARTICLE

Electron nanoprobe induced oxidation: a simulation of direct-write purification

Cite this: DOI: 10.1039/xoxxoooooox

J.D. Fowlkes,[a,b] B. Geier[c], B Lewis[b], P.D. Rack[a,b], M.Stanford[b], R. Winkler[c] and H. Plank[c,d]

Received ooth January 2012,
Accepted ooth January 2012

DOI: 10.1039/xoxxoooooox

www.rsc.org/

Electron beam direct–write has recently taken a large step forward with the advent of methods to purify deposits. This development has opened the door for future direct–write device prototyping and editing. In one such approach, an additional beam scanning procedure removes carbonaceous impurities via oxidation from metal–carbon deposits (e.g., PtC_5) in the presence of H_2O or O_2 after deposition. So far, critical aspects of the oxidation reaction remain unclear; experiments reveal clearly that electron stimulated oxidation drives the process yet it is not understood why H_2O purifies by a bottom–up mechanism while O_2 purifies from the top–down. The simulation results presented here suggest that the chemisorption of dissolved O_2 at buried Pt nanoparticle surfaces controls purification in the top–down case while both the high relative solubility coupled with weak physisorption of H_2O explains the bottom–up process. Crucial too is the role that the carbonaceous contaminant itself has on the dissolution and diffusion of O_2 and H_2O. These results pave the way for simulation driven experiments where (1) the transient densification of the deposit can be accounted for in the initial deposit design stage and (2) the deposition and purification steps can be combined.

Introduction

Direct–write deposition will play a significant role in materials synthesis in the coming years. The rapid advancement of additive manufacturing as a practical means to deposit complex geometric prototypes typifies the power of the direct–write paradigm. Although currently a macroscopic approach, a complementary nanoscale additive manufacturing exists using a focused beams of electrons[1], photons and ions to directly write features on surfaces using either adhesive liquid films[2] or an impinging vapor[1]. These methods are suitable to tackle problems unique to nanofabrication such as the spatially controlled deposition of functional materials on curved surfaces, low temperature processing, 2D materials[3] and/or nanoscale repair solutions. In general, as IC fabrication approaches the atomic scale, the current layer–by–layer, planar assembly model will, at minimum, have to be complemented with the direct–write approach.

Focused electron beam induced deposition (FEBID) is one such method where a focused, nanoscale electron probe is used to dissociate a surface adsorbed precursor molecule in order to accumulate a condensed deposit. Organometallic compounds are commonly used as the

View Article Online
DOI: 10.1039/C5CP01196E
Journal Name

gaseous precursor with the purpose of depositing a typically metallic element. Secondary electrons (SE), liberated from the substrate during electron impact, re–emerge from the surface contributing to the partial fragmentation of physisorbed[4, 5] or chemisorbed[6] precursors. Functional deposits require a controlled chemical composition often necessitating a pure metal. Until recently, EBID was of limited use as a materials synthesis method due to the partial organometallic dissociation[7, 8] - remnant carbon, hydrogen and oxygen ultimately degrade materials properties. A host of methods have emerged over the last 5 years to purify deposits derived from select precursors including *ex–situ* annealing[9], *in–situ* annealing[10], precursor molecules with simpler dissociation pathways[11], atomic radical abatement[12] annealing in reactive atmospheres[10], *in–situ* laser–induced thermal by–product desorption[13] and in–situ electron beam curing in reactive atmospheres[14, 15]. Electron beam–induced etching using H_2O and O_2, in addition to other gases, has been used for both bulk and materials selective etching[16] with the curing process being an example of the later.

In–situ electron beam curing has been shown to remove most residual carbon (>95%)[10, 14, 15] from Pt deposits which are highly contaminated with carbon following deposition (~PtC_{4-8}) providing a powerful, minimally invasive method to purify deposits at room temperature. This later work constitutes a significant step towards pure direct–write and the *in–situ* nature of the method lends itself to future applications. However, the reaction sequence and chemical mechanism during purification is not yet well understood. Also, morphological contraction accompanies purification resulting in unintended shape changes of the deposit. Understanding the entangled transient development of purification and the resulting deposit contraction is thus the goal of this work and which will undoubtedly help pave the way for purification integrated with direct write design. This goal requires an understanding of (1) the role that O_2/H_2O dissolution and diffusion plays in controlling the spatial extent of purification and (2) how the dynamically evolving PtC_x morphology changes the location of the reaction through changes in deposit composition which also affects the electron penetration into the solid. Simulations are ideally suited to interrogate the dynamic interplay of these potentially governing factors.

Here, a hybrid simulation is presented consisting of an electron scattering (Monte Carlo) component[17] that predicts the deposited energy profile in the deposit coupled with a finite difference numerical approach used to solve the transport related differential equations and thus emulate the evolving spatial profiles of Pt, amorphous carbon (aC) and O_2 in the deposit. The chemisorption of dissolved O_2 at nanoparticle surfaces within the deposit is also considered here as a key factor during purification consistent with recent results presented by Sachser et al[18]. In related work, Bishop et al have shown that FEBID via thermally activated chemisorption leads to high deposit purity for SiO_2 deposited from the $Si(OC_2H_5)_4$ (TEOS) precursor without the need for subsequent purification[6]. The aim of this model/simulation is to prove or disprove the assumption that concentrated regions of dissolved oxygen and deposited energy drive purification in the form of the localized production of carbon oxides in the bulk. Without specific knowledge of a reaction mechanism, an empirical reaction model is entertained using a 2nd order reaction constant which depends on (1) the electron energy loss "concentration" and (2) the concentration of a dissolved oxidizing agent. This computational approach disregards the exact chemical nature of the reactants, transition states and products that would be derived from, e.g., the density functional theory (DFT) approach based on electronic structure calculations. Ideally, a full description of the system would require rate equations informed by computational chemistry. DFT has been used to interrogate reactions influenced by dissolved gases[19]

The experimental purification method that inspired this study implements a pulsed electron irradiation strategy by raster beam scanning which must be taken into account by the simulation. *Deposit shape changes occur in concert with the liberation of carbon at a fixed metal content effectively increasing the deposit density in time.* These two points necessitate simulation feedback with repeated/periodic looping of the (1) Monte Carlo and (2) transport simulations to account for the transient deposit densification which couples into transport calculations. The accuracy of simulation results will be tested by comparing final calculations to experimental characteristics such as (1) the deposit thickness contraction rate and (2) the Pt and C composition profile in the thickness dimension of the deposit.

Background

The construction of the purification model was based on experimental observations for the purification of nominal PtC_5 deposits derived from the precursor molecule $MeCpPt^{IV}Me_3$ [14, 20] – an internal morphology consisting of ~2nm Pt nanocrystals embedded in an amorphous carbon matrix (*aC*). The aC phase consists of unreacted precursor fragments mostly containing Pt and C[21] and/or by entirely dissociated precursor fragments which polymerize in the presence of excessive electrons[21, 22]. *The most notable experimental difference occurred when choosing the reactant gas molecule – O_2 induced aC oxidation that started at the deposit surface and proceeded down into the deposit[15] while H_2O induced aC oxidation started at the deposit–substrate interface proceeding upward into the deposit[14].* Some light is shed on these experimental results if the aC is treated as a carbon–based 'polymer–like' material in terms of materials properties. As – deposited PtC_x deposits exhibit significant sp^2 hybridization with $sp^2/sp^3 > 0.5$ often associated with sputtered aC films or glassy carbon[23]. For example, the aC matrix permeability was recognized as a key materials parameter considering that the permeability coefficient (Π) for H_2O is typically 10–100 times larger in magnitude relative to O_2 for a wide range of polymers[24]. Considering that the nominal diffusion coefficient of the two oxidizing agents is roughly the same in polymeric materials, the higher solubility of H_2O, relative to O_2, was conjectured to enable a "deep"

Journal Name View Article Online DOI: 10.1039/C5CP01196E ARTICLE

oxidation reaction while limiting the O_2 process to the near surface region of the deposit. As will be shown, simulation results were consistent with this explanation yet could not entirely explain the demonstrative difference between H_2O and O_2. Specifically, an additional phenomenon was needed to account for the concentration of the purification reaction in the near surface region for the case of O_2 purification.

Initially, the electron–induced reaction was modelled as 2nd order with the rate of purification being proportional to the concentration of deposited electron energy multiplied by the concentration of *mobile dissolved* O_2. Yet, under these conditions, only smooth, continuously changing PtC_x (where x is the atomic content of C atoms per Pt atom) composition gradients could be produced in the thickness dimension of the deposit whereas a highly Pt–rich layer was observed in experiments.

Pt bound atomic oxygen was then considered as an additional mechanism where the bound state is favourable for subsequent electron dissociation – O_2 undergoes dissociative chemisorption (E_a=-3eV/atom) on Pt[25] when impingement occurs from the vapour while H_2O is known to only very weakly adsorb (E_a=-0.3eV/atom) onto Pt surfaces[26, 27]. At room temperature, H_2O exhibits weak, picosecond adsorption residence times at room temperature while the O_2 is fixed over macroscopic timescales. Dissolved gas impingement/trapping on Pt nanoparticle surfaces embedded in the deposit was added to the simulation. This required solving the general adsorption differential equation at each pixel layer within the deposit to account for the dynamically changing PtC_x composition. The addition of the reactant nanoparticle interaction made it possible to concentrate purification at the surface (for the case of O_2). Excluding the interaction led to an interaction isolated at the pad–substrate interface (for the case of H_2O) providing a model of the transient nature of the purification reaction in the context of conventional reaction rate theory.

Experimental Inspiration

Real FEBID purification experiments were conducted in two serial stages consisting of (1) the growth of a rectangular prism followed by (2) a purification step[15]. A typical prism geometry was 500nmx500nm in the substrate plane (xy–plane) and a 100nm thickness (z–dimension). The relevant experimental conditions are provided in tabular form in **S1** with electron imaging and composition related results available in [14, 20]. The electron beam size (10–50nm) is much smaller than the cumulative lateral deposit size requiring a beam scan over the surface to produce the desired deposit dimensions. The growth process is conducted using a looping tactic where a nanoscale thick layer of deposit is produced and sequential looping yields an accumulating deposit in the z–dimension. The looping pattern is discretized into a series of pixels (1–10nm). The focused electron probe dwells at a given pixel within the looping pattern for a fixed dwell time (τ_d) and then proceeds to the next pixel. A row scan, column advance pattern (raster) was used during both growth and the purification step[15] where the electron beam size is on the order of tens of nanometers.

The purification procedure follows deposition (**figure 1**). Although the purification problem is treated as 1D (depth coordinate) in the model of purification to follow, it is important to note that the model was informed by a Monte Carlo simulation of beam scanning implemented in 3D (**figure 2**). **S2** shows a representative movie of the simulated beam scanning for a single purification loop in order to provide a clear description of the beam scanning routine. As a result, energy is received at any given point (x,y) in the deposit as a series of pulses. For example, **figure 3** shows the deposited beam energy, integrated in the depth coordinate at the center pixel of the deposit, for all beam coordinates during a single purification scanning loop. Returning to experiments, a constant flux of O_2/H_2O molecules impinges on the deposit surface during scanning which subsequently dissolves and diffuses into the deposit volume. A capillary nozzle was used to supply O_2 gas to the deposit surface at an impingement rate of $7.17x10^3$ molecules/nm^2 s. The surface pressure (P) of O_2 was 2mTorr. Conversely, an environmental SEM was used for the H_2O experiments where the surface flux was $3.58x10^5$ molecules/nm^2 s (P=75mTorr).

Experimental results indicate that the penetrating electrons stimulate an oxygen reaction that consumes the aC matrix. The assumption is made that carbon is liberated from the precursor deposit seemingly through the production of CO and/or CO_2 gas which are well known by–products for the Pt–C–O system[28]. Owing to the fact that the deposit exhibits volume contraction during purification indicates that the liberated carbon oxide diffuses to the surface of the deposit and subsequently desorbs from the deposit surface into the vacuum. Nonetheless, the ratio of the oxidation by-products CO and CO_2 are currently unknown for the case of oxidation at buried Pt nanoparticles in aC with dissolved O_2. It is assumed here that equals parts CO and CO_2 are produced during purification. $CO_{1.5}$ is used as the simulated by–product.

Model (Physical Chemistry)

Simulations revealed that a mechanism akin to atomic layer deposition (ALD) reproduces experimental results for the case of O_2 purification. Whereas conventional ALD occurs at the substrate–vapor interface, here the reaction is localized at buried metal nanoparticle surfaces. In place of heat, the electron–beam stimulates the 2nd half reaction. In conventional Pt ALD using the precursor *(MeCp)Pt^{IV}Me$_3$* the first half–reaction consists of introducing O_2 to a Pt film[29]. The relevant reaction here consists of buried Pt nanoparticles exposed to dissolved O_2 gas;

ARTICLE View Article Online DOI: 10.1039/C5CP01196E Journal Name

$$2Pt_{np} + O_{2(dissolved)} \rightarrow 2[Pt_{np} - O] \quad [1]$$

where Pt_{np} refers to Pt atoms at the nanoparticle surface and [Pt_{np}–O] refers to a chemisorbed state. In this paper, the dissociative chemisorption of O_2 into atomic O is assumed to spontaneously occur at unoccupied embedded *Pt* nanoparticle surfaces upon contact driven by O_2 diffusion. The aC is treated as a homogeneous and continuous medium which facilitates the transport of O_2 to the Pt nanoparticle surface. Further, we assume that the Pt nanoparticle surface area is available for adsorption by the O_2 ignoring any effects associated with the aC-Pt interface – only the coverage of atomic O on the Pt nanoparticle surface impacts the probability of adsorption. Without exact knowledge of the sticking coefficient of *dissolved* O_2 on buried Pt nanoparticles the vapor phase value of 0.05 is used following previous estimations [30, 31]. During the 2nd conventional ALD half–reaction[29] has provided the qualitative reaction;

$$MeCp(Pt^{IV})Me_3(g) + [Pt - O_x] \rightarrow Pt + CO_{2(g)} + H_2O(g) + by - products \quad [2]$$

In this case, adsorbed O reacts with impinging $MeCp(Pt^{IV})Me_3$ yielding Pt accumulation as well as a host of vapor compounds. The reaction ensues at an elevated temperature in the range 200–350 ^oC[29, 32]. Here, the self–limiting nature of the known ALD reaction is translated into a maximum allowable surface coverage of a monolayer for O chemisorbed on Pt nanoparticles. A modified 2nd half–reaction is proposed here;

$$3[Pt_{np} - O] + 2C \xrightarrow{eV} 3Pt_{np} + 2CO_{1.5(g)} \quad [3]$$

where the carbon C is part of the *aC* matrix and in contact with *Pt* nanoparticles reacts with bound, atomic O in response to the deposition of energy by inelastic electron scattering yielding $CO_{1.5}$ dissolved in the *aC*. The observed volume contraction of the deposit leads to an increase in the Pt nanoparticle density as $CO_{1.5}$ is liberated as well as annihilation of the complementary void in the aC. Nonetheless, it is also possible that liberated *atomic* Pt in the aC matrix, as a result of this reaction, may migrate to larger buried Pt nanoparticles leading to embedded nanoparticle growth as a function of time driven by surface free energy minimization. Our model takes into account the former and ignores the later mechanism. Sachser et al have observed accelerated Pt purification as the Pt grain size increases from transient conductance measurements[18]. This increases the surface area for further oxygen chemisorption yet at the expense of CO desorption which is effectively interrupted by the denser oxygen coverage. It is important to note that the role of O_2 during the conventional ALD of Pt is not yet fully understood[29] and nonetheless the base model referenced above is well accepted.

Model (Mathematical)

O_2 gas dissolves in the *aC* phase of the deposit according to Henry's Law at a concentration equal to $P\times\Pi/D_{o2}$ where P is the surface pressure of O_2 impinging at the surface and is constant and D_{O2} is the diffusion coefficient of O_2 in *aC*. The time–dependent mobile oxygen concentration C^m_{O2} in the *aC* is described by equation 4;

$$\frac{\partial C^m_{O_2}(z,t)}{\partial t} = D_{O_2}\frac{\partial^2 C^m_{O_2}(z,t)}{\partial z^2} - \delta\,\Phi_{O_2}(C^m_{O_2}, r_{np}, z, t)\left[4\pi r^2_{np}(z,t)\rho_{np}(z) - \frac{C^{im}_O(z,t)}{s_d}\right] + \frac{C^{im}_O(z,t)}{2\tau} \quad [4]$$

where, from left–to–right and term–by–term is described the diffusion of mobile O_2 in the *aC*, the chemisorption of O_2 as bound atomic O on unoccupied embedded Pt nanoparticle surface area which is subtractive from the mobile population of O_2 and finally the spontaneous associative desorption of 2xO to form O_2 *(which is additive in O_2)*. **S3** provides details on the development of both equations 4 and 5. **Table 1** summarizes the variables in equations 4 and 5. The transient behaviour of the bound atomic oxygen concentration is described by equation 5;

$$\frac{\partial C^{im}_O(z,t)}{\partial t} = -kC_{eV}(z,t)C^{im}_O(z,t) + 2\delta\,\Phi_{O_2}(C^m_{O_2}, r_{np}, z, t)\left[4\pi r^2_{np}(z,t)\rho_{np}(z) - \frac{C^{im}_O(z,t)}{s_d}\right] - \frac{C^{im}_O(z,t)}{\tau} \quad [5]$$

and adsorption is limited to a monolayer of coverage. The immobile atomic oxygen concentration facilitates the electron–driven purification reaction according to the 1st term which leads to the direct formation of gaseous carbon oxide ($CO_{1.5}$). The inelastic energy deposited in the PtC_x by the primary electron beam was taken as the fraction associated with secondary electron (SE) creation and is represented in the calculations as a concentration C_{eV} which has units of eV/m^3. Although the final discussion of results below will argue in favour of mechanism better described by a "cross–section", the fact that the local temperature may influence dissociation cannot be ruled out. **S4** contains information on how C_{eV} is mathematically derived from Monte Carlo simulations as well as a physical interpretation relating the 2nd order reaction constant (k) used above and the total electron impact dissociation cross–section often associated with FEBIP. $CO_{1.5}$ is assumed to desorb, diffuse and vaporize from the deposit surface without influencing dissociation or O coverage. Experiments reveal that the deposit contracts at a rate of approximately 1 monolayer per 100ms of processing time. The contraction rate is directly proportional to

Journal Name View Article Online DOI: 10.1039/C5CP01196E ARTICLE

the rate of $CO_{1.5}$ vaporization so effectively one monolayer is lost per loop (*1 loop = 98ms during O_2 purification*). As a result, at any given time the concentration of $CO_{1.5}$ within the deposit is negligible. This in turn indicates that the $CO_{1.5}$ surface coverage on buried Pt nanoparticles is negligible and can be ignored as a factor that influences atomic oxygen coverage.

Electron induced dissociation in the chemisorbed state has been considered previously[6]. The 2nd and 3rd terms are reproduced from equation 4 except from the point–of–view of atomic *O*. *Regarding the 1st term, once the atomic O is consumed in this manner it is deemed chemically "activated" and the assumption is made that this species (O*) instantly reacts with aC yielding* $CO_{1.5}$ (without actual knowledge of the ratio of CO and CO_2 by–product yields, parity was assumed with $2C + 3O^* \rightarrow 2CO_{1.5}$ with $CO_{1.5}$ representing a mixture of CO and CO_2). For context in the thermal coordinate, Sachser et al. explained that CO is the sole product during thermal annealing of Pt in the presence of O_2 at 420K[18]. Here we assume that *C* is liberated from the aC matrix at a rate governed by equation 6

$$\frac{\partial C(z,t)}{\partial t} = -\frac{2}{3} k C_{eV}(z,t) C_O^{im}(z,t) \quad [6]$$

which can be converted into a volume of carbon removed per unit time by multiplication with the voxel volume (Δz^3) and the atomic volume of amorphous carbon (Ω_{aC}).

Results & Discussion

As–deposited thin film rectangular prisms consist of Pt nanoparticles randomly distributed in a polymer–like, *aC* matrix. The simulations of oxidation in O_2 reported here were inspired by real experiments conducted using a primary beam energy of 5keV, a beam current setting of 120pA and a dwell time per pixel of 10μs to deposit the initial pad[20]. TEM characterization of pads deposited under these conditions has revealed a Pt nanoparticle density of 3.25×10^{-2}np/nm^3 and a mean Pt nanoparticle radius of ~1nm[21]. These parameters yield a nominal deposition composition of $PtC_{5.05}$ which is consistent with the composition measured using energy dispersive spectroscopy[21, 33]. Thus, the initial morphological condition for subsequent simulations was set as a homogeneous $PtC_{5.05}$ (referred to hereafter as PtC_5) composition in the z–coordinate where the starting pad thickness was 100nm.

Initial purification simulations were executed with the goal of (1) replicating the experimentally observed rate of vertical pad contraction per growth loop while (2) simultaneously emulating the PtC_x composition profile. The most influential simulation parameters were the oxygen diffusion coefficient in pad, the *aC* solubility parameter (S) and the reaction rate constant k, were varied in order to converge on the experimentally defined metrics. The first significant revelation of the simulation was the observation that the experimental PtC_x thickness profile could not be achieved using a dissociation model where the electron energy loss concentration directly dissociates *mobile O_2 dissolved* in the *aC* matrix. Experimental PtC_x during purification yield a Pt–rich region at the surface that grows at a rate of ~2.5nm/min for the used parameters followed by a steep gradient in composition that asymptotically approaches the initial ~PtC_5 composition with depth[20]. It was impossible to concentrate enough dissolved O_2 in the near surface region to replicate this profile. For example, in one scenario, very small values of D_{O2} made it possible to concentrate dissociation at the surface but also yielded a purification rate that was an order of magnitude less than the experimentally observed rate. Simply increasing Π led to non–physical values. This issue was resolved by changing the reaction model.

An updated reaction model, the dissociative chemisorption of atomic oxygen on embedded Pt nanoparticles made it possible to concentrate oxygen locally – *the distinct chemical potential of the bound oxygen, relative to the dissolved molecular form, provided a chemical pathway to concentrate oxygen especially considering the high surface area to volume ratio of the nanoparticles with 1nm initial radii*. Supplementary materials describe the key aspects of this model and its translation into a numerical simulation including (**S5**) the internal oxygen flux at embedded nanoparticle surfaces and (**S6**) the incorporation nanoparticle size effects into the simulation such as nanoparticle growth as purification evolves.

Real experiments using O_2 for combustion purification reveal a nearly linear purification rate as a function of the number of scanning loops [14, 15, 20]. This result made it possible to initially explore a large number of simulation parameters quickly by executing only single loop of purification and extrapolating this purification rate to the experimentally determined growth rate. This provided a significant time savings reserving longer simulations for only meaningful parameter sets.

Figure 4 shows the results for a host of single loop purification computer experiments targeted to investigate the effect of internal oxygen binding on PtC_x composition changes (5keV 1800pA, **S1**). Materials parameters are provided in **Table 2**. Each curve represents an independent computer experiment where the only difference is τ. The curve itself represents the pixel contraction observed as a function of depth of the pad $\Delta z(z)$ which is an indicator of carbon loss as a function of depth. Moreover, each curve

View Article Online
DOI: 10.1039/C5CP01196E
Journal Name

has been normalized to the maximum and minimum contraction in order to demonstratively highlight the composition changes and the location of the purification. A smaller number in the range *0–1* indicates more contraction and thus more *aC* liberation as $CO_{1.5}$. Normalization was necessary for illustration purposes because, as shown in the **figure 4 inset**, the total deposit thickness contraction for each case varied significantly from curve–to–curve. The initial PtC_5 surface is located at 100nm and the SiO_2 interface at 0nm.

Within the limits of realistic simulation parameter ranges (see **S7**), a set of parameters could not be found that satisfied the following criteria simultaneously (1) total contraction rate per loop (*~10pm/loop*) and (2) the experimentally observed composition profile (*top-down*) assuming that *mobile* O_2 was dissociated – the no Pt binding condition. For example, the red curve (**figure 4**) yields a purification concentrated in the deposit interior at 65 nm, not concentrated at the surface as seen in experiments. In addition, the purification rate is prohibitively slow at only 0.43 pm/loop (as will be shown later, a rate of ~30pm./loop is required in the initial stages of purification to yield the *average* rate of 10pm/loop for real experiments). *However, by introducing the dissociative chemisorption of atomic O on embedded Pt nanoparticle surface area both problems could be reconciled simultaneously*. Including the bound atomic O state required the introduction of a mean surface residence time for O on Pt nanoparticle surfaces (**S3**). **Figure 4** shows the effect of increasing τ. Again, the bound state is required for dissociation in the model. The contraction rate is increased while the purification was simultaneously localized to occur at the surface, i.e., the transition from τ= 10μs to 100μs shows this change clearly (**figure 4**). In light of these promising results, it is important to note these primary assumptions made in constructing this model.

1. Adsorption properties normally used to characterize the vapour–surface interaction apply also for dissolved solute–solid interactions.
2. Bound *O* has a distinctly different chemical potential than O_2 making it possible to concentrate oxygen above the solubility limit.
3. Mobile O_2 dissociation is ignored in the model in favour of bound O.

In order, assumption #1 is made on 'good faith' alone and thus is the weakest assumption in our proposed model until proven otherwise, there exists precedent in the literature for assumption #2, regarding for example H_2 storage[34], and assumption #3 has similarities with ALD whereas here the assumption is made that the concentration of electron energy loss, in the form of secondary electrons, drives the dissociation process.

The results shown in **figure 4** for τ=10–25ms were found to best emulate experimental results – a concentrated top down process was found with the correct long term deposit contraction rate. Proceeding further, a simulation was carried out for the entire *7000* loops using τ=12.5ms and is described next.

A weakly sub–linear purification process was found that converged to the 10pm/loop thickness reduction rate from the initially high rate of 33pm/loop. Moreover, the transient $PtC_{x(z)}$ profiles simulated are also consistent with experiments. **Figure 5a** shows an atomic ratio map (*C* per *Pt*) of the deposit, sampled every 40 scanning loops, for the 7000 loop simulation. The surface plot may be interpreted as a transient view of the deposit composition in cross–section with *Pt*–rich regions being relatively brighter. The electron energy loss profile in the deposition changes drastically in response to purification. **Figure 5b** shows the evolution of energy deposited in the pad as a function of time. The energy has been normalized to the maximum energy (E_{im}) in the E(z) profile during the 1^{st} purification loop. In this way, the energy ratio shows the relative amplification of energy deposition as purification evolves. Although energy loss is initially concentrated midway into the deposit, the oxygen concentration gradient across the deposit ultimately limits the reaction to the surface. Purification at the surface ensues in the form of Pt enrichment which acts to shift the inelastic energy deposited toward the dense surface region. These results highlight the importance of including simulation feedback between the Monte Carlo electron scattering and transport simulations. The quality of the parameter set to yield the correct solution is now discussed in terms of (1) uniqueness, (2) agreement with additional experiments and (3) compared with H_2O–based experiments.

The uniqueness of the parameter set underpinning the solution presented in **figure 5** was tested by conducting approximately 400 single loop purification simulations in (D_{O2}–S–*k*) space. The relevant parameter space was defined as $D_{O2} = 1x10^{-2}$–$1x10^{+1}$ μm^2/s, $S = 1x10^{-4}$–$1x10^{+1}$ molecules/nm^3/Torr and $k = 1x10^{+2}$–$1x10^{+4}$ nm^3/eV/s based on parameters assembled from the literature **S7** [24]. Solution quality was accessed based on the condition min($|\Delta h_{sim}–\Delta h_{exp}|$) where Δh is the single loop contraction rate **S8**. Five of the 10 best solutions fell within a physically meaningful parameter range. These 5 solutions also fell within 5% of Δh_{exp} exhibiting statistical variations of D_{O2}=3.8±1.9μm^2/s, S=0.03±0.01molecules/nm^3/Torr, $k=1.2x10^{+4}±8x10^{+3}$nm^3/eV/s.

The reaction constant (k) for the physical model presented is [**S7**];

Journal Name View Article Online DOI: 10.1039/C5CP01196E ARTICLE

$$k = 4\pi D_{O_2}^{eff} \Delta r \quad [8]$$

where D_{O2}^{eff} is the effective diffusion coefficient of O_2 which includes the effect of diffusion *and chemisorption*. Δr is interpreted as the cumulative interaction radius for bound oxygen and an electron. This expression does not appear explicitly in equation 5 above but is applicable from a fundamental point–of–view. *Importantly, D_{O2}^{eff} remains effectively static 350–380nm^2/s [S5] for a wide range of D_{O2} values 0.1-10 μm^2/s because the time to diffuse between nanoparticles in the aC ($\rho_{np}^{-2/3}$/6D) ~10^{-4}ms is 5 orders–of–magnitude lower than the mean residence time of O on the nanoparticle surface at ~10ms*. The minimum interaction radius anticipated was the radius of oxygen (~0.3nm) while the maximum was taken as a secondary electron mean free path of 2.5nm yielding a *k* range of 2x10^{+2} – 5x10^{+3} nm^3/eV/s. **Figure 6** shows that a reaction constant magnitude less than the specified range of *k* yields a contraction rate consistent with experiments yet fails to produce a top–down purification – the reaction proceeds slow enough to allow O_2 diffusion deep into the deposit driving a bottom–up process. Conversely, at relatively high values of *k*, the reaction takes places so fast that Pt surface enrichment rapidly densifies the near surface region localizing the inelastic electron energy loss and limiting electron penetration into the bulk.

The parameters supplied in **Table 2** also recovered the per loop thickness contraction rate found for a primary electron beam voltage study spanning 5–20 keV as reported previously in[35].

Purification experiments conducted using H_2O were shown to occur from the bottom–up with Pt concentrated at the buffer/deposit interface[14]. This is consistent with the 'fast' gas characteristic attributed to H_2O due to its relatively large values of Π and D in polymers[36]. Simulations were prepared which also emulated the H_2O experimental conditions reported in **S1**. H_2O parameters were estimated by using the parameters determined for O_2 (**Table 2**) except that Π was increased by 16 times for H_2O in order to replicate the average ratio of Π H_2O/O_2 for a host of polymers[24]. Examining first the experimental conditions, a significant difference to note was the reactant surface pressure which was 2mTorr for the O_2 case versus 75mTorr for H_2O. Regarding properties, H_2O–Pt adsorption can be ignored in this case and only dissolved mobile H_2O is dissociated (see the Background section above). The permeability coefficient is typically 100 times larger for H_2O compared with O_2 for glassy polymers[24]. The reaction constant (*k*) for H_2O was set equal to the determined value for O_2 due to a lack of knowledge regarding the internal cross–section and the fact that the electron impact dissociation cross–sections for O_2 and H_2O[37] differ by less than an order–of–magnitude. Under these constraints, the simulation replicated the bottom–up experimental finding as shown in **figure 7**.

The enhanced H_2O dissolution and transport leads to a bottom–up purification process (**figure 7a**). In this case, electron energy loss is initially concentrated also in the middle of the film but shifts down toward the deposit/substrate interface (**figure 7b**). It is important to note that the gas pressure was higher for the complementary H_2O experiments 75mTorr, relative to the 2mTorr used in the O_2 experiment, yet an additional simulation performed using 75mTorr O_2 still yielded a top–down process emphasizing the importance of the gas selection.

The permeability coefficient (Π) recovered from SxD_o is nearly constant for all quality solutions (**S9**). The 2x10^{-10} (cm)(cm^3 STP)/(cm^2 Pa s) value is typically associated with rubbery polymers but is also characteristic of a glassy polymer material with dissolved voids. Indeed, porous EBID deposits have been confirmed for as–deposited EBID Pt structures in the past[14]. Fundamentally, Henry's law includes the combined processes of gas impingement, adsorption and dissolution in the solid: voids are disregarded. In this circumstance, the dual sorption model[38, 39] shows promise and may be added to the simulation in the future. Moreover, in reality, Π must be time–dependent and decreasing for a purification process as voids annihilate during densification. The refined value of D_{O2} also suggests a glassy carbon *aC* matrix **S7**.

Lastly, the absorption energy (-3eV/atom)[25] of atomic O on Pt suggests our best simulation solution should most probably involve an infinite mean residence time (τ) at RT. Electron stimulated desorption provides a possible explanation for the finite time of 25ms. Notably, O desorption begins above 300 ^oC[29, 31, 40] during conventional Pt ALD.

Conclusions

Focused electron beam induced deposition (FEBID) is commonly used to deposit a wide range of nanoscale metallic geometries for nanofabrication prototyping/repair. In general, FEBID yields highly impure metallic deposits containing spatially distributed metallic nanoparticles embedded in an amorphous phase containing mostly carbon. In order to expand the future direct–write prototyping capability of FEBID will require complementary purification methods to yield the requisite material atomic composition. Post deposition, beam stimulated oxidation at RT using both O_2 and H_2O has been shown to remove the *aC* yet the mechanisms were not well understood. Simulation results provided in this paper, for widely used PtC_x deposits from *MeCp(Pt^{IV})Me$_3$* FEBID, suggest that for O_2, electron energy loss stimulates oxidation concentrated around embedded Pt

View Article Online
DOI: 10.1039/C5CP01196E
Journal Name

nanoparticles with chemisorbed oxygen, not just localized at the deposit surface. In favour of this model are realistic values for the permeability coefficient, diffusion coefficient and reaction rate which imitate both the experimentally observed rate of carbon liberation from the deposit as well as the steep PtC_x composition profile, in the thickness dimension, with Pt–rich regions located in the near surface region (top–down) Conversely, H_2O yields a Pt–rich region at the bottom of the deposit explained, in part, by the large permeation of H_2O in addition to the weak H_2O–Pt nanoparticle interaction – combining these effects, H_2O penetrates deeply for subsequent dissociation. Nonetheless, the large number of variables, both known and unknown, combined with the three main assumptions regarding the interaction at the dissolved O_2–embedded Pt nanoparticle interface preclude an exact determination of parameters. Regardless, the simulation results are bolstered by a robust parameter search yielding a single space of best solutions. Moreover, continual feedback between the evolving deposit density, inelastic electron energy loss and spatial distribution of reactant were required to capture transient features in purification experiments for O_2 and H_2O.

Methods

Numerical methods

A Monte Carlo electron scattering simulation implementing the single scattering method[41] was used to calculate the inelastic electron energy loss per voxel in a 3D spatial domain consisting of a variable PtC_x composition where (x) varies in the thickness dimension (z) and in time. The deposit was supported on an SiO_2 buffer layer and Si substrate.

An explicit time marching finite differencing method was used to solve the 1D parabolic diffusion equation for the case of O_2 diffusion in the depth dimension of the $PtC_{x(z,t)}$ deposit. The grid spacing in this particular simulation was time–dependent and the Taylor series expansion method used to derive the numerical approximation is described here as well as in[42]. The improved Euler method (Heun's method) was used to approximate the 1st order differential equation describing the time–dependent surface coverage of atomic oxygen on nanoparticle surface area. Both the diffusion and coverage numerical estimates were made simultaneously on the same time step (Δt) and 1D contracting spatial grid $\Delta z(z,t)$.

Variable mesh spacing and the explicit finite differencing scheme

One characteristic of the electron beam facilitated purification process is the contraction of the deposit as carbon is liberated from the deposit. Deposit contraction impacts the diffusion transport properties. This attribute was incorporated into the simulation by choosing a finite difference method to solve the diffusion equation coupled with variable grid spacing. Solving the following two truncated Taylor series expansions for the 2nd derivative in mobile O_2 concentration;

$$C_{O_2}^m(z+\delta z_+) = C_{O_2}^m(z) + \delta_{z+}\frac{\partial C_{O_2}^m(z)}{\partial z} + \frac{\delta_{z+}^2}{2}\frac{\partial^2 C_{O_2}^m(z)}{\partial z^2} + \cdots \quad [7]$$

$$C_{O_2}^m(z-\delta z_-) = C_{O_2}^m(z) - \delta_{z-}\frac{\partial C_{O_2}^m(z)}{\partial z} + \frac{\delta_{z-}^2}{2}\frac{\partial^2 C_{O_2}^m(z)}{\partial z^2} + \cdots \quad [8]$$

yields;

$$\frac{\partial^2 C_{O_2}^m(z)}{\partial z^2} = \frac{\delta_{z-}C_{O_2}^m(z+\delta_{z+}) + \delta_{z+}C_{O_2}^m(z-\delta_{z-}) - (\delta_{z+}+\delta_{z-})C_{O_2}^m(z)}{\delta_{z-}\frac{\delta_{z+}^2}{2} + \delta_{z+}\frac{\delta_{z-}^2}{2}} \quad [9]$$

where $\delta_{\square}$ indicates a forward or reverse displacement in the z–coordinate. The displacement between each z–coordinate is related to the actual pixel width (Δz) by;

$$\delta_{z+} = \frac{\Delta z(q+1)}{2} + \frac{\Delta z(q)}{2} \quad [10]$$

$$\delta_{z-} = \frac{\Delta z(q)}{2} + \frac{\Delta z(q-1)}{2} \quad [11]$$

where q is the z–coordinate index. This approach is advantageous for two reasons. First, the pixel width decreases in proportion to the amount of carbon lost in the reaction step but the number of platinum atoms is constant. Thus, the number of platinum atoms does not have to be updated providing a computational savings and the thickness reduction is directly related to carbon loss. In addition, the Monte Carlo simulation domain has a fixed voxel size requiring only that the atomic content of each voxel be updated as shown in **figure 8** by a grid

View Article Online
DOI: 10.1039/C5CP01196E ARTICLE

projection and averaging method when overlayed with the shrinking 1D transport grid. Lastly, **S10** provides a map of the simulation program flow.

Acknowledgements
JDF and PDR acknowledge that the creation of the model and simulation were conducted at the Center for Nanophase Materials Sciences, which is a DOE Office of Science User Facility. BG, RW and HP gratefully acknowledge the valuable support provided from Prof. Dr. Ferdinand Hofer. BG, RW and HP also acknowledge financial support by the COST action CELINA (Nr. CM1301), EUROSTARS project TRIPLE-S (Nr. E! 8213) and the bmvit exchange program. MGS acknowledges support from the National Defense Science and Engineering Graduate Fellowship funded through the AFOSR. BBL acknowledges support via the University of Tennessee Chancellor's Fellowship program.

Notes and references
[a] Nanofabrication Research Laboratory, Center for Nanophase Materials Sciences, Oak Ridge National Laboratory, Oak Ridge, Tennessee 37831, United States
[b] Materials Science and Engineering Department, The University of Tennessee, Knoxville, Tennessee 37996, United States
[c] Graz Centre for Electron Microscopy, Steyrergasse 17, 8010 Graz, Austria.
[d] Institute for Electron Microscopy and Nanoanalysis, Graz University of Technology, Steyrergasse 17, 8010 Graz, Austria

† Footnotes should appear here. These might include comments relevant to but not central to the matter under discussion, limited experimental and spectral data, and crystallographic data.

Electronic Supplementary Information (ESI) available: [details of any supplementary information available should be included here]. See DOI: 10.1039/b000000x/

1. I. Utke, P. Hoffmann and J. Melngailis, *J Vac Sci Technol B*, 2008, **26**, 1197-1276.
2. E. U. Donev and J. T. Hastings, *Nano Lett*, 2009, **9**, 2715-2718.
3. A. G. Fedorov, S. Kim, M. Henry, D. Kulkarni and V. V. Tsukruk, *Appl Phys a-Mater*, 2014, **117**, 1659-1674.
4. J. A. Spencer, S. G. Rosenberg, M. Barclay, Y. C. Wu, L. McElwee-White and D. H. Fairbrother, *Appl Phys a-Mater*, 2014, **117**, 1631-1644.
5. J. D. Wnuk, J. M. Gorham, S. G. Rosenberg, W. F. van Dorp, T. E. Madey, C. W. Hagen and D. H. Fairbrother, *J Phys Chem C*, 2009, **113**, 2487-2496.
6. J. Bishop, C. J. Lobo, A. Martin, M. Ford, M. Phillips and M. Toth, *Phys Rev Lett*, 2012, **109**.
7. A. Botman, J. J. L. Mulders and C. W. Hagen, *Nanotechnology*, 2009, **20**.
8. J. D. Wnuk, S. G. Rosenberg, J. M. Gorham, W. F. van Dorp, C. W. Hagen and D. H. Fairbrother, *Surf Sci*, 2011, **605**, 257-266.
9. A. Botman, J. J. L. Mulders, R. Weemaes and S. Mentink, *Nanotechnology*, 2006, **17**, 3779-3785.
10. S. Mehendale, J. J. L. Mulders and P. H. F. Trompenaars, *Nanotechnology*, 2013, **24**.
11. K. L. Klein, S. J. Randolph, J. D. Fowlkes, L. F. Allard, H. M. Meyer, M. L. Simpson and P. D. Rack, *Nanotechnology*, 2008, **19**.
12. J. D. Wnuk, J. M. Gorham, S. G. Rosenberg, T. E. Madey, C. W. Hagen and D. H. Fairbrother, *J Vac Sci Technol B*, 2010, **28**, 527-537.
13. N. A. Roberts, C. M. Gonzalez, J. D. Fowlkes and P. D. Rack, *Nanotechnology*, 2013, **24**.
14. B. Geier, C. Gspan, R. Winkler, R. Schmied, J. D. Fowlkes, H. Fitzek, S. Rauch, J. Rattenberger, P. D. Rack and H. Plank, *J Phys Chem C*, 2014, **118**, 14009-14016.
15. H. Plank, J. H. Noh, J. D. Fowlkes, K. Lester, B. B. Lewis and P. D. Rack, *Acs Appl Mater Inter*, 2014, **6**, 1018-1024.
16. M. Toth, *Appl Phys a-Mater*, 2014, **117**, 1623-1629.
17. D. A. Smith, J. D. Fowlkes and P. D. Rack, *Nanotechnology*, 2007, **18**.
18. R. Sachser, H. Reith, D. Huzel, M. Winhold and M. Huth, *Acs Appl Mater Inter*, 2014, **6**, 15868-15874.
19. A. Kakanakova-Georgieva, G. K. Gueorguiev, S. Stafstrom, L. Hultman and E. Janzen, *Chem Phys Lett*, 2006, **431**, 346-351.
20. B. B. Lewis, M. G. Stanford, J. D. Fowlkes, K. D. Lester, H. Plank and P. D. Rack, *submitted*, 2014.
21. H. Plank, G. Kothleitner, F. Hofer, S. G. Michelitsch, C. Gspan, A. Hohenau and J. R. Krenn, *J Vac Sci Technol B*, 2011, **29**.
22. H. Plank, T. Haber, C. Gspan, G. Kothleitner and F. Hofer, *Nanotechnology*, 2013, **24**.
23. S. Frabboni, G. C. Gazzadi and A. Spessot, *Physica E*, 2007, **37**, 265-269.
24. W. D. Callister, Jr. and D. G. Rethwisch, *Materials Science and Engineering: An Introduction*, Wiley, 2014.
25. E. M. Karp, C. T. Campbell, F. Studt, F. Abild-Pedersen and J. K. Nerskov, *J Phys Chem C*, 2012, **116**, 25772-25776.
26. G. S. Karlberg, *Phys Rev B*, 2006, **74**.
27. S. Meng, E. G. Wang and S. W. Gao, *Phys Rev B*, 2004, **69**.
28. M. Mundschau and B. Rausenberger, *Platinum Metals Review*, 1991, **35**, 188-195.
29. T. Aaltonen, M. Ritala, T. Sajavaara, J. Keinonen and M. Leskela, *Chem Mater*, 2003, **15**, 1924-1928.

View Article Online
DOI: 10.1039/C5CP01196E
Journal Name

30. D. R. Monroe and R. P. Merrill, *J Catal*, 1980, **65**, 461-469.
31. C. T. Campbell, G. Ertl, H. Kuipers and J. Segner, *Surf Sci*, 1981, **107**, 220-236.
32. M. Hiratani, T. Nabatame, Y. Matsui, K. Imagawa and S. Kimura, *J Electrochem Soc*, 2001, **148**, C524-C527.
33. R. Winkler, B. Geier and H. Plank, *Appl Phys a-Mater*, 2014, **117**, 1675-1688.
34. K. J. Jeon, H. R. Moon, A. M. Ruminski, B. Jiang, C. Kisielowski, R. Bardhan and J. J. Urban, *Nat Mater*, 2011, **10**, 286-290.
35. B. B. Lewis, M. G. Stanford, J. D. Fowlkes, K. Lester, H. Plank and P. D. Rack, *Beilstein J Nanotech*, 2015, **6**, 907-918.
36. Y. Yampolskii, I. Pinnau, B. D. Freeman and S. Matteucci, *Transport of Gases and Vapors in Glassy and Rubbery Polymers, in Materials Science of Membranes for Gas and Vapor Separation*, John Wiley & Sons, 2006.
37. Y. Itikawa and N. Mason, *J Phys Chem Ref Data*, 2005, **34**, 1-22.
38. A. S. Michaels, J. A. Barrie and W. R. Vieth, *J Appl Phys*, 1963, **34**, 13-&.
39. J. C. Guo and T. A. Barbari, *Macromolecules*, 2009, **42**, 5700-5708.
40. Y. Ohno and T. Matsushima, *Surf Sci*, 1991, **241**, 47-53.
41. D. C. Joy, *Scanning Microscopy*, 1991, **5**, 329-337.
42. M. G. Stanford, B. B. Lewis, J. H. Noh, J. D. Fowlkes, N. A. Roberts, H. Plank and P. D. Rack, *Acs Appl Mater Inter*, 2014, **6**, 21256-21263.

View Article Online
DOI: 10.1039/C5CP01196E

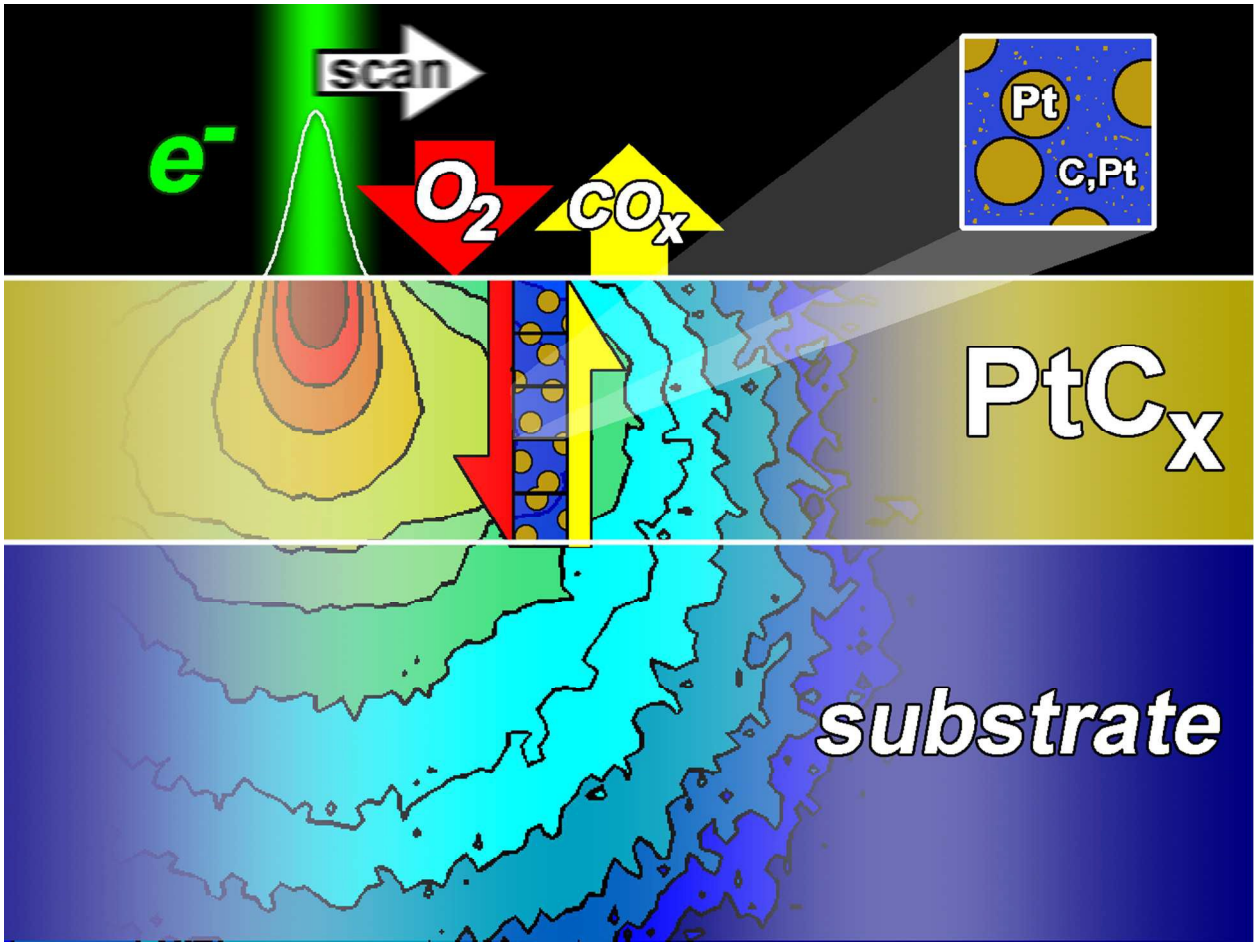

Figure 1 A schematic illustration of the electron beam induced purification process shown in cross-section. The penetrating electron beam stimulates the reaction of dissolved oxygen with residual carbon buried within the deposit. In the proposed model, inelastic energy transfer from the primary electron beam to the PtC_x deposit triggers a reaction between atomic oxygen (O) bound at platinum (Pt) nanoparticle surfaces and the amorphous carbon matrix. Atomic O is created when O_2 diffuses into the deposit and chemisorbs onto Pt nanoparticle surfaces. The electron spatial distribution in the solid as well as the diffusion of oxygen exhibits the largest gradient in the z-dimension reducing the transport problem to 1D for the relatively thin deposit geometries investigated. The electron beam scanning produces a dynamic electron energy distribution in the solid film.

View Article Online
DOI: 10.1039/C5CP01196E

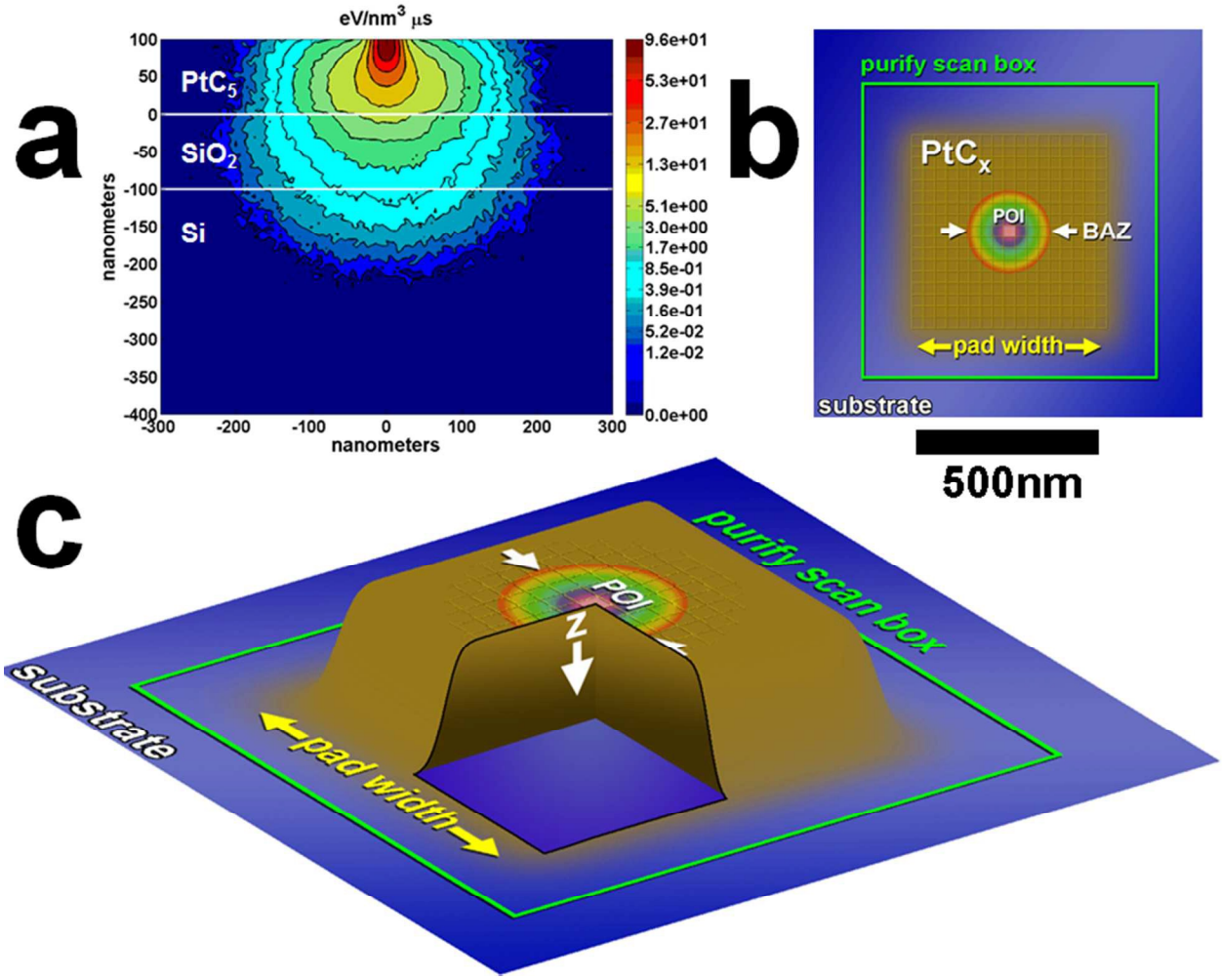

Figure 2 (a) Inelastic energy deposition in the $PtC_5/SiO_2/Si$ film stack during a static electron beam exposure. For this example a beam dwell time of 5.92μs was used. The electron beam characteristics were 5keV, 1600pA and a Gaussian profile with a FWHM = 25nm. (b) A schematic illustration of the purification geometry from the top-down perspective (x-y plane). The purification domain is defined by the square shaped, green boundary (edge length = 620nm). The electron beam defined in (a) is scanned through this region in either a (1) raster or (2) serpentine digital pattern. The dwell time defines the electron beam residence time per pixel. The actual deposit (gold region) also has a square shape but is smaller as defined by the pad width (edge length = 500nm). A pixel-of-interest (POI) lies at the pad center. The electron beam has a finite interaction region as shown in (a) and therefore only deposits significant energy at the POI when the beam rests at a dwell pixel contained within the beam affected zone (BAZ). The first step of the simulation process is a 3D Monte Carlo electron trajectory simulation. Inelastic electron-energy loss is accumulated at the POI, in the depth (z–coordinate), when the electron beam, shown in (a), is scanned through one loop of the simulation domain in a raster fashion. The grid overlay (in gold) shows a representative square array of beam dwell pixels. (c) A cross-sectional view of the deposit geometry. The thickness of deposit is 100nm as defined in the cross-section view in (a). Inelastic energy deposition by the

View Article Online
DOI: 10.1039/C5CP01196E

electron beam during raster is stored in the voxels located in the z-dimension as a function of time to later inform a 1D transport simulation that considers oxygen permeation, diffusion, binding and an electron stimulated reaction with the amorphous carbon matrix.

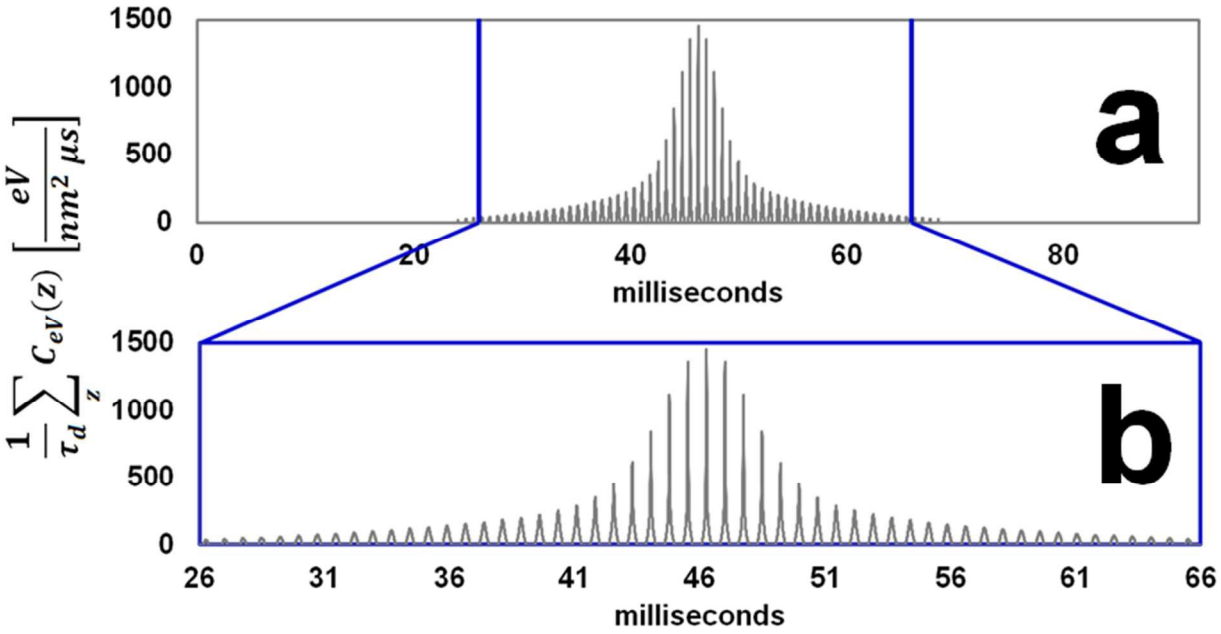

Figure 3 (a) The integrated energy concentration (C_{eV}) deposited *in the center* of a 300nm x 300nm PtC_5 deposit during a single purification loop. The integration was performed at the pixel–of–interest (POI) in the thickness dimension of the PtC_5 deposit which was 100nm thick. This process is described in S2. The beam dwell time per pixel was 25.5μs. The pixel size, or beam displacement, was 5nm. The FWHM of the primary electron beam was 25nm. The center of the deposit is defined as the stack of voxels located below the pixel-of-interest (POI) *located at (x=0, y=0)*. The primary beam raster pattern shown in Figure S2(a) was used to create energy concentration profile. Thus, each time data point corresponds to a particular (x,y) beam position in the 2D beam raster and represents the contribution of the electron interaction volume generated in the bulk to the energy deposited at the center stack of voxels. This is described in Figures S2(b-c). Periods of low electron flux, where the beam is positioned relatively far from the center, the beam interaction volume fails to intersect the position (x=0,y=0) voxel z-stack which facilitates the refresh of O_2 into the bulk of the deposit.

View Article Online
DOI: 10.1039/C5CP01196E

Table of variables

$E_o = primary\ electron\ beam\ energy\ [eV]$

$i_o = primary\ electron\ beam\ current\ \left[\frac{C}{s}\right]$

$\tau_d = electron\ beam\ dwell\ time\ per\ pixel\ [s]$

$D_{O_2} = diffusion\ coefficient\ of\ O_2 in\ amorphous\ carbon\ (aC)\ \left[\frac{m^2}{s}\right]$

$P = gas\ pressure\ at\ the\ deposit\ surface\ [mTorr]$

$\tau = mean\ residence\ time\ of\ O_2\ on\ buried\ Pt\ nanoparticle\ surfaces\ [s]$

$\delta = sticking\ probability\ of\ O_2 on\ buried\ Pt\ nanoparticle\ surfaces\ (0-1)$

$\Phi_{O_2} = diffusive\ flux\ of\ O_2 striking\ buried\ Pt\ nanoparticle\ surfaces\ \left[\frac{molecules}{m^2\ s}\right]$

$C_{O_2}^{m}(z,t) = concentration\ of\ mobile\ O_2 in\ the\ amorphous\ carbon\ (aC)\ \left[\frac{molecules}{m^3\ s}\right]$

$C_{O}^{im}(z,t) = concentration\ of\ immobile\ atomic\ O\ bound\ to\ Pt\ nanoparticle\ surfaces\ \left[\frac{molecules}{m^3\ s}\right]$

$C_{eV}(z,t) = concentration\ of\ deposited\ electron\ energy\ in\ the\ deposit\ \left[\frac{eV}{m^3}\right]$

$k = reaction\ constant\ for\ electron\ stimulated\ oxidation\ \left[\frac{m^3}{eV\ s}\right]$

$r_{np(o)} = initial, mean\ radius\ of\ Pt\ nanoparticles\ [m]$

$r_{np}(z,t) = mean\ radius\ of\ Pt\ nanoparticles\ [m]$

$\rho_{np} = Pt\ nanoparticle\ density\ \left[\frac{np}{m^3}\right]$

$\sigma_{np}(z,t) = surface\ area\ of\ Pt\ nanoparticles\ per\ voxel\ [m^2]$

$s_d = atomic\ oxygen\ (O)\ binding\ sites\ per\ unit\ Pt\ surface\ area\ \left[\frac{O\ sites}{m^2\ np}\right]$

$\Delta x = voxel\ edge\ length\ (Monte\ Carlo\ electron\ scattering\ simulation)[m]$

$\Delta z(z,t) = pixel\ thickness\ (transport\ simulation)[m]$

$\Pi = permeability\ coefficient\ of\ O_2\ in\ amorphous\ carbon\ \left[\frac{(cm)(cm^3 STP)}{(cm^2\ Pa\ s)}\right]$

$S = solubilty\ of\ O_2 in\ amorphous\ carbon\ \left[\frac{molecules}{m^3\ Torr}\right]$

Nomenclature

$aC = acronym\ used\ when\ referring\ to\ amorphous\ carbon\ matrix$

$PtC_5 = average\ composition\ of\ deposit\ before\ purification$

$PtC_x = depth\ dependent\ composition\ during\ purification$

$Pt_{np} = Pt\ atoms\ at\ the\ surface\ of\ a\ Pt\ nanoparticle$

$Pt_{np} - O = chemisorbed\ atomic\ O\ on\ a\ Pt\ atom\ at\ the\ surface\ of\ a\ Pt\ nanoparticle$

$CO_{1.5} = mean\ composition\ of\ assumed\ reaction\ by-product$

Table 1 Variables critical to the simulation including materials properties, electron beam settings and gas properties as well as nomenclature

View Article Online
DOI: 10.1039/C5CP01196E

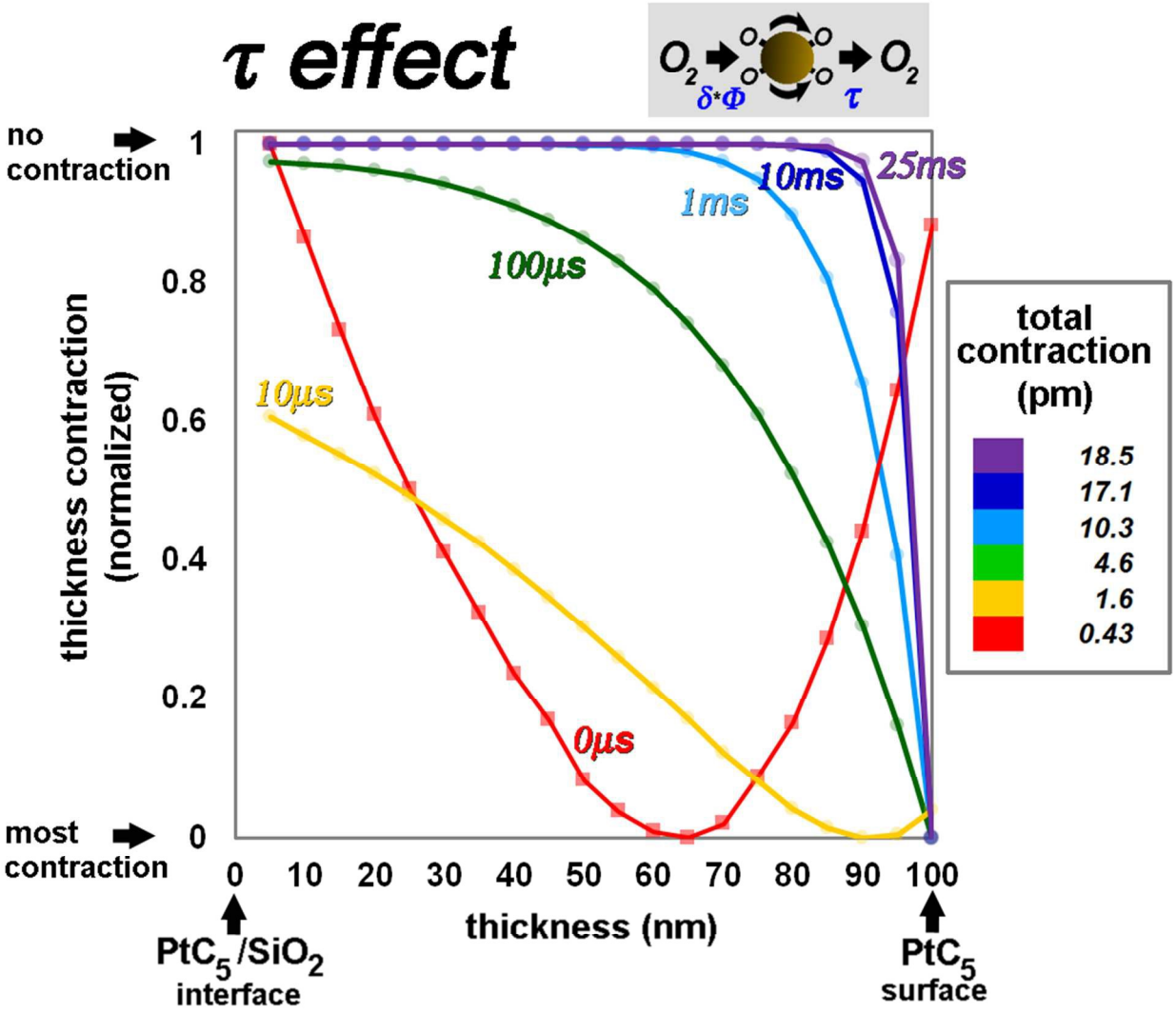

Figure 4 Thickness contraction (purification) as a function of PtC_5 thickness following a single loop of purification in O_2 using a primary beam energy of 5keV, a beam current of 1600pA and

View Article Online
DOI: 10.1039/C5CP01196E

reaction constant of k=4000 $nm^3/eV\ s$. The experimental conditions reported in **S1** for O_2 were used along with the variable settings provided in **Table 2**. The study shows the effect of varying the mean residence time (τ) of atomic oxygen on buried *Pt* nanoparticle surfaces for six different residence times. The initial pixel thickness was 5nm for each pixel. Thickness contraction represents the loss of amorphous carbon (*aC*) at that particular depth. The initial PtC_5 pad surface is located at 100nm. The thickness contraction has been normalized to the maximum and minimum values to amplify the change in thickness/composition for each experiment. The total deposit thickness change for each case is shown in tabular form at right. The electron beam driven dissociation of *dissolved* molecular oxygen (red curve) mimics the integrated electron energy loss profile (**S2**). However, (*aC*) loss was unrealistically low in terms of absolute deposit contraction per loop as shown in the table (34pm/loop was consistent with experiments for the early stages of contraction). In the alternative dissociation model, which considers the electron stimulated dissociation of bound atomic oxygen (*O*), an increase in mean *O* residence time has the effect of concentrating the purification at the surface and increasing the overall purification per loop. Mean residence time values are superimposed where applicable.

View Article Online
DOI: 10.1039/C5CP01196E

Table of variables

$PtC_{5.05}$
$h = 100nm$
$D_{O_2} = 4\ \mu m^2/s$
$\tau = 0 - 25ms$
$\delta = 0.05$
$\Phi_{O_2}(r_{np(o)}, D_{O_2}, C_{O_2}^m = 6x10^{-5}O_2/nm^3) = 3.4x10^3\ collisions/nm^2/s$
$k = 4x10^3 nm^3/eV/s$
$r_{np(o)} = 1nm$
$\rho_{np} = 3.25x10^{-2} Pt\ nanoparticles/nm^3$
$s_d = 8\ oxygen\ sites/nm^2$
$\Delta x = 5nm$
$\Pi = 1.8x10^{-10}\ (cm)(cm^3 STP)/(cm^2 Pa\ s)$
$S = 3x10^{-2} molecules/nm^3/Torr$

Table 2 Simulation parameters required to mimic the 5keV, 1800 pA experimental data set for the case of immobile oxygen dissociation driven by the focused electron beam. These values represented the solution. The origins of these values are found in **S7**.

View Article Online
DOI: 10.1039/C5CP01196E

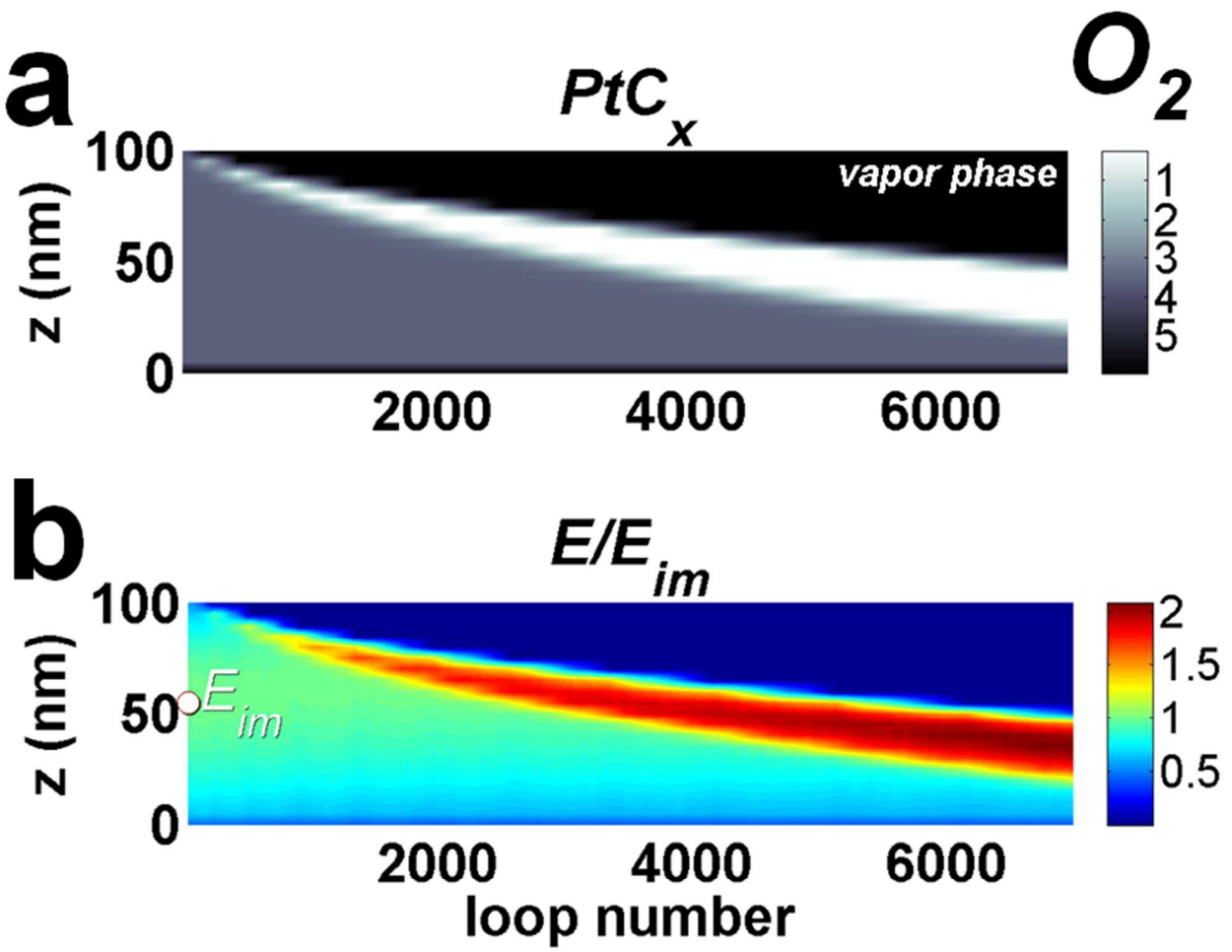

Figure 5 (a) PtC_x composition profile after 7000 loops of purification in 2mTorr O_2 which emulates the experimental conditions reported in **S1** and the variables provided in **Table 2** with τ=12.5ms The y-coordinates spans the initial deposit thickness with the initial surface at 100nm and the substrate interface at 0nm. The x-axis is the loop number. Pt enrichment occurs in a thin layer at the surface (white region) which thickens with increased purification time. This is consistent which morphological changes observed in real experiments. The color bar is displayed in atoms C per Pt atom. (b) The deposited energy profile in the thickness coordinate at the POI, integrated per loop. The data has been normalized to the depth of maximum energy deposition during the first purification loop indicated by E_{im}. The color bar values indicate the magnitude of E/E_{im}. In this way, the enhanced electron energy loss in the near surface layer in evident as a function of time as well as the shift from the center of the deposit to the surface.

View Article Online
DOI: 10.1039/C5CP01196E

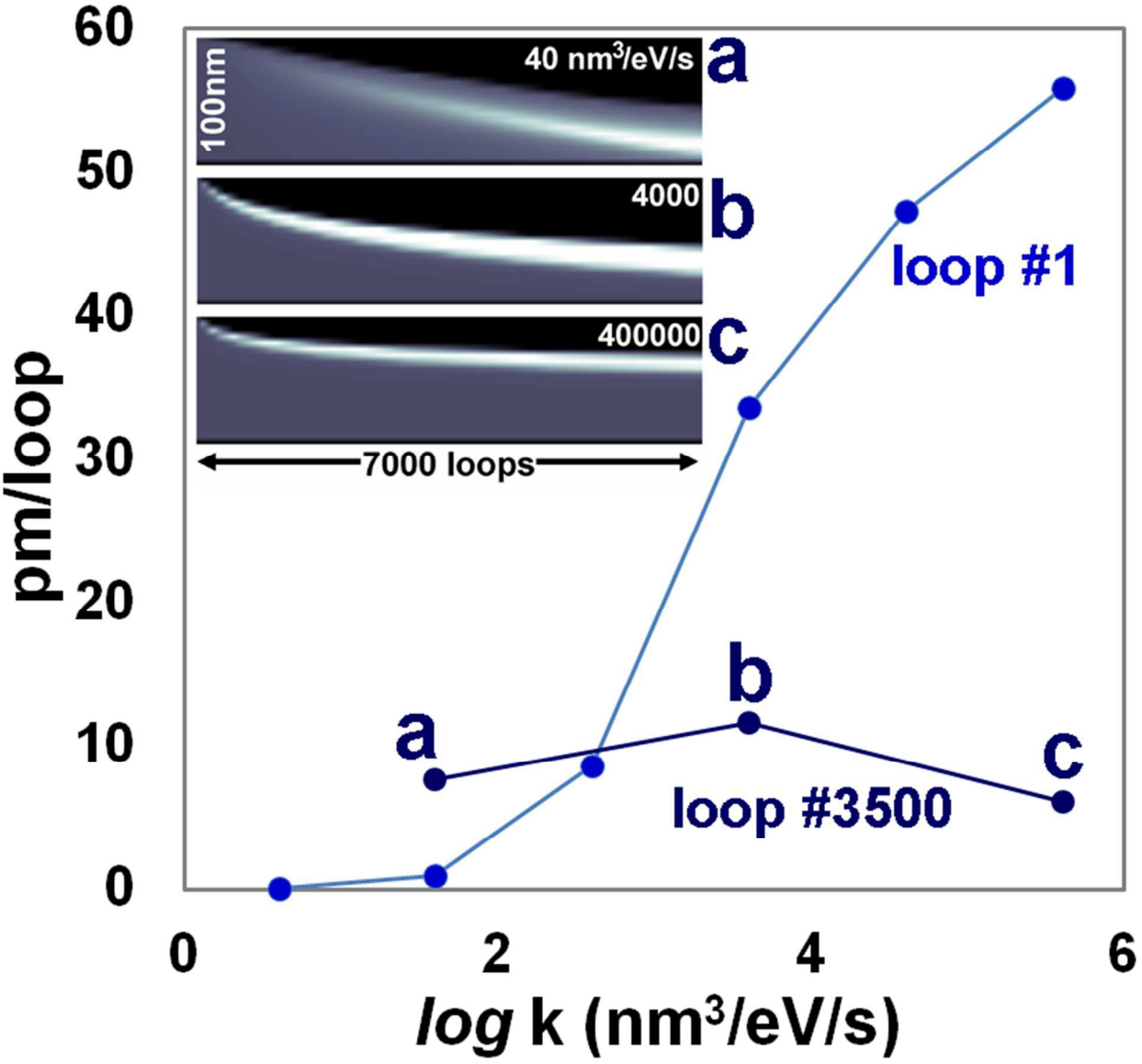

Figure 6 The reaction rate constant (k) impacts the rate of purification and the PtC_x thickness profile in the deposit during O_2 purification. The average deposit contraction rate is shown on the y–axis while the x–axis is the rate constant describing the electron stimulated reaction. The simulation of purification was performed at 5keV and 1600 pA according to the experimental conditions presented in **S1** for O_2 and the variables provided in **Table 2** with τ=12.5ms Single loop purification experiments (light blue curve) tailored to explore the variable k show the typical transition from an electron limited regime toward, at a relatively low value of k, a mass–transport limited regime at large k. Superimposed slices of the $PtC_{x(z)}$ profile during 7000 loops of purification show the evolution of a complex process where a bottom–up purification occurs at low k (indicated by the bright, Pt–rich region at the base of the deposit) while the total integrated C yield per electron actually decreases at large values of k because the surface localized inelastic electron energy loss in the rapidly evolving Pt–rich surface layer prevents electron penetration into the bulk.

View Article Online
DOI: 10.1039/C5CP01196E

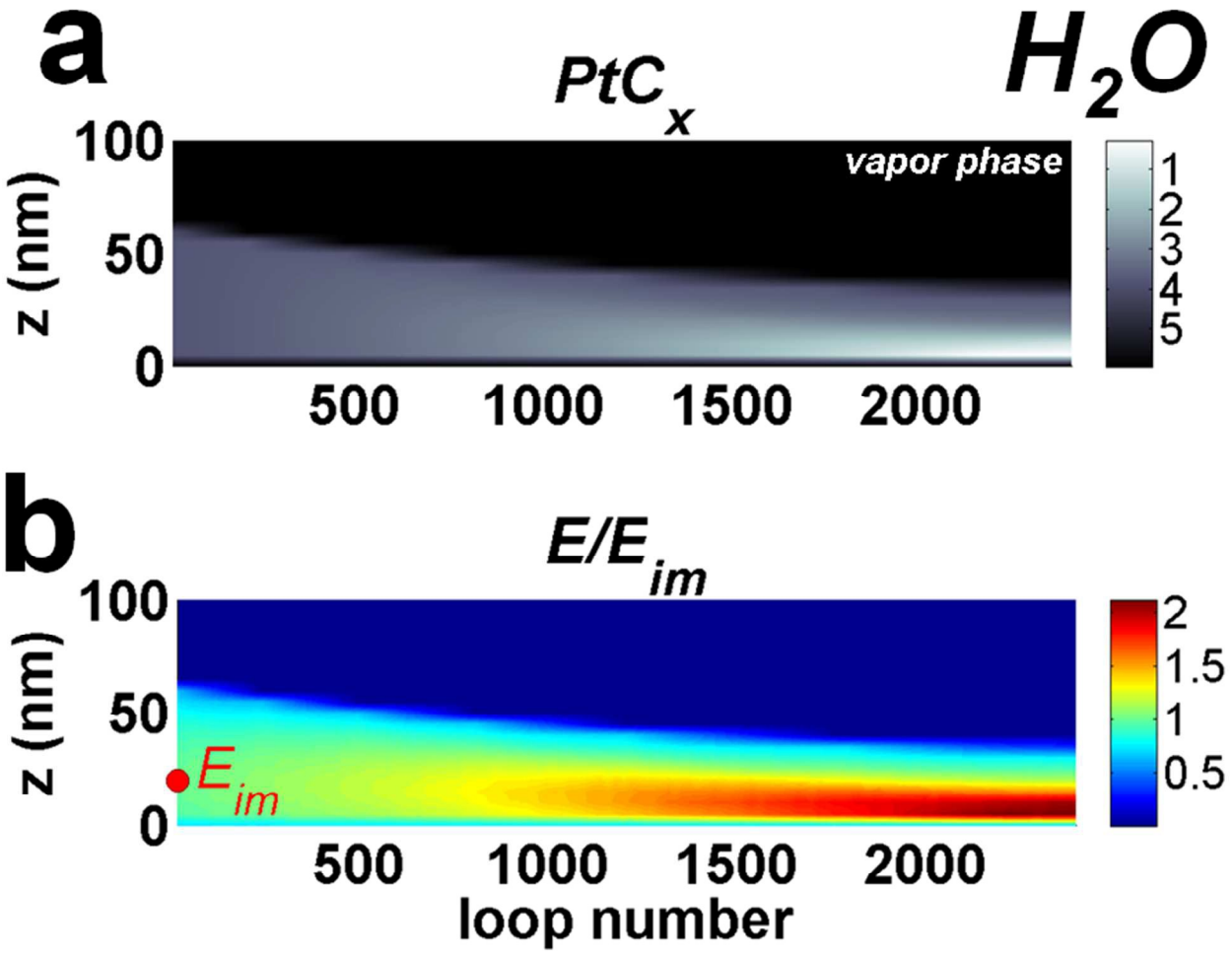

Figure 7 (a) PtC_x composition profile after 2400 loops of purification in 75mTorr H_2O which emulates the experimental conditions reported in **S1** for H_2O. *H_2O-Pt binding is weak and therefore ignored*. Instead, the direct dissociation of dissolved, mobile H_2O was considered to drive purification but using the same reaction constant as O_2 (k=4000 $nm^3/eV/s$) in order to isolated the effect of enhanced H_2O solubility which was □=0.5 molecules/nm^3/Torr a value 16x larger than for O_2 see **S7**. The y-coordinate spans the initial deposit thickness with the initial surface at 60nm and the substrate interface at 0nm. The x-axis is the loop number. Pt enrichment occurs in a thin layer at the buffer-deposit (white region) which thickens with increased purification time. This is consistent which morphological changes observed in real experiments. The color bar is displayed in atoms C per Pt atom. (b) The deposited energy profile in the thickness coordinate at the POI, integrated per loop. The data has been normalized to the depth of maximum energy deposition during the first purification loop indicated by E_{im}. The color bar values indicate the magnitude of E/E_{im}. In this way, the enhanced electron energy loss in the near surface layer in evident as a function of time as well as the shift from the center of the deposit to the surface.

View Article Online
DOI: 10.1039/C5CP01196E

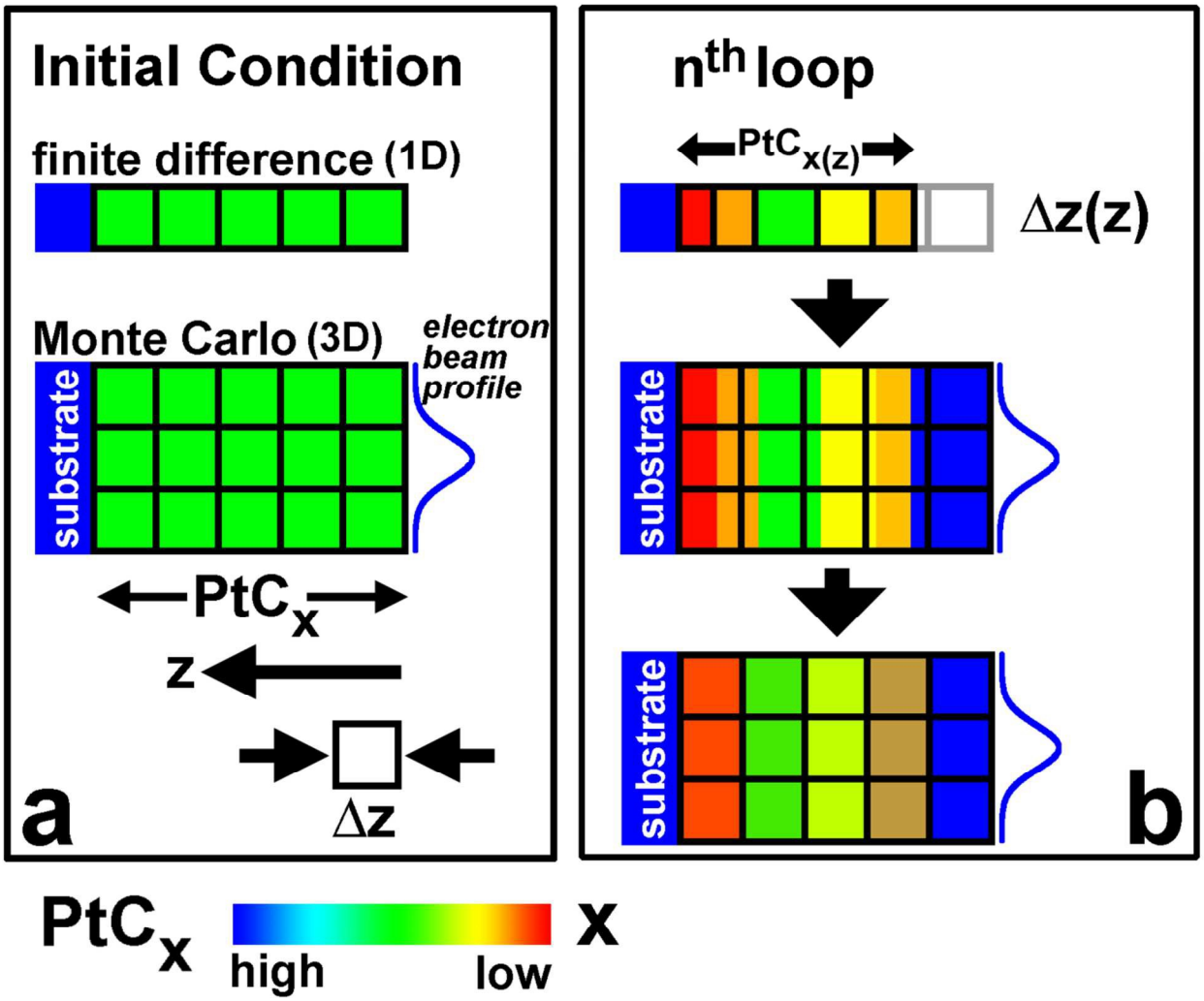

Figure 8 The basic simulation structure consists of an iterative process where a Monte Carlo simulation generates the inelastic electron energy distribution as a function of depth (z–dimension) in the deposit. Next, a continuum simulation is executed that emulates gas permeation, bulk diffusion, reactant adsorption at buried Pt nanoparticle surfaces and the electron driven reaction. These phenomenon all act in concert to change the composition profile in time. The new composition is fed back to the Monte Carlo simulation after a User specified number of purification loops. This schematic illustrates this iterative process; (a) The 1D finite difference domain (indicated by the single row of pixels) that calculates reaction–diffusion starts with a uniform PtC_x atomic ratio (see the composition scale at the bottom of the figure). The pixel thickness (Δz) is a function of time in this domain. Conversely, the pixel thickness in the Monte Carlo domain (indicated using multiple rows in the scheme) is fixed. The primary electron beam spatial profile is shown to indicate the surface (blue Gaussian trace). (b) Carbon is liberated from the deposit in time which results in deposit contraction in the z-coordinate. In the Monte Carlo simulation, the composition of a voxel is updated to reflect the updated $PtC_{x(z)}$ composition profile in the z-dimension, by projecting the composition from the

View Article Online
DOI: 10.1039/C5CP01196E

contracting domain onto the static Monte Carlo grid. For illustration purposes, an example is shown with enhanced purification located in the center of the deposit. Specifically, average density, molecular weight and atomic number per voxel are updated in the Monte Carlo domain. Thus, the effective “surface” in the Monte Carlo simulation remains fixed and voxel parameters change to account for material parameter changes.